Journal of Materials Science & Technology 233 (2025) 280–288

Contents lists available at ScienceDirect

Journal of Materials Science & Technology

journal homepage: www.elsevier.com/locate/jmst

Research Article

Two-dimensional hybrid nanosheets towards room-temperature organic ferrimagnetic semiconductor

Xiaoling Men[a,b], Fei Qin[a,b], Bo Zhang[c], Kangkang Yao[d], Yin Zhang[d], Yangtao Zhou[a], Qifeng Kuang[a,b], Xiaolei Shang[a,b], Ruiqi Huang[a,b], Zhiwei Li[c], Sen Yang[d], Gang Liu[a,b], Teng Yang[a,*], Da Li[a,b,*], Zhidong Zhang[a]

[a] Shenyang National Laboratory for Materials Science, Institute of Metal Research, Chinese Academy of Sciences, Shenyang 110016, China
[b] School of Materials Science and Engineering, University of Science and Technology of China, Shenyang 110016, China
[c] School of Physical Science and Technology, Lanzhou University, Lanzhou 730000, China
[d] School of Physics, MOE Key Laboratory for Nonequilibrium Synthesis and Modulation of Condensed Matter, Xi'an Jiaotong University, Xi'an 710049, China

ARTICLE INFO

Article history:
Received 14 November 2024
Revised 7 January 2025
Accepted 6 February 2025
Available online 22 March 2025

Keywords:
Two-dimensional nanosheets
Organic-inorganic hybrid material
Ferrimagnetic semiconductor
Magnetic properties
Semiconducting properties

ABSTRACT

Organic magnetic semiconductors have aroused much attention for spintronic applications. However, it remains challenging to achieve organic semiconductors with strong room-temperature ferromagnetism. Here, we report a two-dimensional (2D) tetragonal organic-inorganic ferrimagnetic (FIM) semiconductor of $Fe_{14}Se_{16}(peha)_{0.7}$ (peha = pentaethylenehexamine) with excellent thermal stability and a Curie temperature (T_C) higher than 519 K. Magnetic and Mössbauer measurements reveal a long-range magnetic ordering in single crystalline $Fe_{14}Se_{16}(peha)_{0.7}$ nanosheets. The saturation magnetization and coercivity are 5.9 emu g^{-1} and 0.42 kOe at 5 K, which slightly reduces to 4.6 emu g^{-1} and ~0 Oe at 300 K. A direct optical bandgap of 2.22 eV is obtained by tuning electronic structure of β-Fe_3Se_4 host layers through spacer layers consisting of Fe^{3+} and peha. Electrical and Seebeck coefficient data indicate that the n-type semiconductor follows the thermally-activated conduction mechanism ($\ln\rho \propto T^{-1}$) in a range of 130–300 K with an activation energy (E_a) of 62.69 meV. Thermal conductivity is 2.5 W m^{-1} K^{-1} at 300 K, while the Wiedemann–Franz law is strongly violated according to electrical-thermal transport data due to weak incorporation of organic spacer layers and host layers. This study sets the stage for exploiting new room-temperature organic magnetic semiconductor systems for spintronic materials.

1. Introduction

Magnetic semiconductors have attracted much interest in spintronic devices for next generation of large-scale integrated electrocircuits [1–4]. Despite mutual modulations of magnetism, electricity and optical properties, room-temperature applications of magnetic semiconductors are bottlenecked by working temperatures lower than room temperature [5]. Although rigorous conditions, such as lattice-matched substrates, ultra-high vacuum, MBE or PLD devices, are required for the preparation of 2D inorganic magnetic semiconductors, in recent years intrinsic room-temperature 2D ferromagnetic (FM) semiconductors show a great prospect for spintronic devices. The bipolar all-electric control of charge and spin was realized in an FM semiconductor $Cr_2Ge_2Te_6$ by adjusting solid-state gate voltages [6]. A build-in electric field in a sandwich-like structure $B(CN)_4/Cr_2I_6/NH_4$ significantly enhances the Curie temperature (T_C) of CrI_3 up to about 105 K [7], while for Cr_2Te_3 flake a T_C increases from 160 K to 280 K as the thickness reduces from 40.3 nm to 7.1 nm [8]. First-principles calculations guide to search Janus crystals as FIM semiconductors with direct band gap and T_C of 1.19 eV and 387 K for $Cr_2Br_3S_3$ and 0.61 eV and 447 K for $Cr_2I_3S_3$, respectively [9]. 2D inorganic magnetic semiconductors are rarely reported on high T_C values and excellent oxidation resistance except $CoFe_2O_4$ [10]. In comparison, organic-inorganic semiconductors with flexibility, low density and well-defined morphology possess excellent optical and electrical properties. The band gap and exciton binding energy of layered organic-inorganic semiconductors are dependent on quantum confinement dominated by the number (n = 1, 2, 3) of inorganic layers. Compared to the band gap of ZnSe (2.5 eV) [11], band gaps of double-layered 2D (Zn_2Se_2)(n-butylamine) and single-layered 2D (ZnSe)(n-butylamine) are blue shifted by 1.0 and 1.6 eV, respectively. Mn-doping induces a strong

* Corresponding authors.
E-mail addresses: yangteng@imr.ac.cn (T. Yang), dali@imr.ac.cn (D. Li).

https://doi.org/10.1016/j.jmst.2025.02.031
1005-0302/

emission band at 585 nm in $(Zn_{0.85}Mn_{0.15}Se)(diethylenetriamine)_{0.5}$ nanobelts and Mn^{2+}-Mn^{2+} magnetic interactions are sensitive to the coordination environment [12]. It suggests that metal ions in complexes can bring ferromagnetism into an organic semiconductor [13]. The highest magnetic ordering temperature of Cu-based organic-inorganic hybrid semiconductors is 34 K [14–17]. In theory, a T_C was predicted to be 560 K for 2D Cr-pentalene organometallic frameworks [18].

Organic semiconductors with a relatively lower thermal conductivity than inorganic materials endow more unique properties and functionalities for organic spintronic devices [19]. Utilizing organic-inorganic hybrid magnetic semiconductors to replace FM electrodes may be an efficient way to avoid the mismatched conductivity between FM electrodes and organic semiconductors that limits the spin injection efficiency [20]. Charge carrier transport in conductive systems is always accompanied with charge and heat. Generally, the total thermal conductivity (κ) of a material is a sum of electronic thermal (κ_{el}) and lattice thermal (κ_{lat}) conductivities. In the diffusive regime, the electronic contribution (κ_{el}) of thermal conductivity is ruled by the Wiedemann–Franz (W-F) law of $\kappa_{el} = \sigma L_0 T$ with the Lorenz number $L_0 = \frac{\pi^2}{3}(\frac{k_B}{e})^2$, a universal constant, independent of material parameters, where σ is the electrical conductivity, T the absolute temperature and k_B the Boltzmann constant. The W-F law is valid in ordinary materials at high and very low temperatures because electron transports are controlled by both the charge and the thermal energy, while the W-F law is invalid in complicated systems where a large range of Lorenz number (L) values, a few-fold to 10^4-fold increase of L/L_0, were reported experimentally [21–23]. In theory, varied carrier concentration, energetic disorder and electric field would lead to a strong violation of the W-F law in organic semiconductors [21]. A correlation between the κ_{el}, κ_{lat} and σ is crucial for spintronic applications of organic magnetic semiconductors.

Variable antiferromagnetic (AFM) Fe_xSe fragments [24] and organic Fe-amine complexes [25–29] provided a favorable hybrid material basis for multifunction and flexible structures. Previously, organic-inorganic $(\beta\text{-}Fe_3Se_4)_4[Fe(triethylenetetramine)_{1.5}]$ insulate nanosheets show a ferrimagnetism with Curie temperature and thermal stability higher than 530 K [25]. $(Fe_2^{2+}Fe_1^{3+}Se_4^{2-})_4[Fe^{2+}(tepa)]Fe^{2+}$ (tepa = tetraethylenepentamine) has a room-temperature saturation magnetization (M_S) up to 4 emu/g and a two-dimensional variable range hopping (VRH) conduction behavior in ~110–300 K range [30]. As Fe^{2+} in spacer layers are replaced by high-spin Fe^{3+}, $(Fe_{2.5}^{2+}Fe_{0.5}^{3+}Se_4^{2-})_4[Fe^{3+}(tepa)]Fe^{3+}$ possesses an enhanced M_S value of up to 7.2 emu g^{-1} at 300 K and a record-high T_C (>560 K) due to a 3D long-range AFM interaction of interlayer and intralayer high-spin Fe^{3+} and Fe^{2+} in the hybrid lattice [31]. When a long-range ferrimagnetic order is suppressed by a reduced content of tepa in spacer layers and a charge transfer gets to ~$0.25e^-/Fe_{0.75}Se$ from organic spacer layer, both the Meissner effect and a resistance drop are observed in $Fe_{14}Se_{16}(tepa)_{0.8}$ below ~42 K [30]. Recently, a 2D organic-inorganic room-temperature multiferroic, $Cr(h\text{-}fpyz)_2$ was designed according to a molecular orbital-mediated magnetic coupling mechanism and an effect of the organic molecule on magnetic coupling type between metal ions [32]. Moreover, potential room-temperature organic-inorganic ferromagnetic semiconductors are reported in theoretical and experimental studies [33–36]. Because Fe^{3+} in complexes are six-coordinated, nitrogen atoms in peha molecules would occupy six equatorial vertices of octahedral Fe^{3+} coordination environment. A charge transfer between inorganic $\beta\text{-}Fe_3Se_4$ host layers and organic Fe^{3+}(peha) spacer layers may provide an opportunity to tune electronic structure to integrate semiconducting properties into an organic-inorganic magnetic material (Fig. S1 in Supplementary Information). 2D organic-inorganic magnetic semiconductors are expected owing to high magnetic ordering temperatures and thermal properties for room-temperature applications.

Here, we report an organic-inorganic room-temperature FIM n-type semiconductor, $Fe_{14}Se_{16}(peha)_{0.7}$ built by $\beta\text{-}Fe_3Se_4$ superstructures and spacer layers consisting of iron ions and organic peha molecules, with a direct E_g of 2.22 eV and an E_a of 62.69 meV. A room-temperature M_S of 4.6 emu g^{-1} strongly supports the robust room-temperature ferrimagnetism of $Fe_{14}Se_{16}(peha)_{0.7}$. The tetragonal FIM semiconductor has excellent thermal stability up to 519 K and thus its T_C should be higher than 519 K. A pellet of $Fe_{14}Se_{16}(peha)_{0.7}$ shows a low thermal conductivity of 2.5 W m^{-1} K^{-1} at 300 K, which is only twice of that of SiO_2, suggesting a potential integration of the organic FIM semiconductor with silicon-based semiconductor materials in future.

2. Experimental

2.1. Materials

Commercially available reagents including iron acetylacetonate ($Fe(acac)_3$, 98 %) and SeO_2 (powder, 99.9 %) were purchased from Aladdin reagent company (Shanghai, China). Peha ($C_{10}H_{28}N_6$, 99.5 %) was purchased from Macklin Company (Shanghai, China), while isopropanol (≥99.7 %) and acetone (99.8 %) were purchased from Sinopharm Chemical Reagent Co. Ltd. (Shenyang, China). All chemicals were used as received without any further purification.

2.2. Synthesis of $Fe_{14}Se_{16}(peha)_{0.7}$ nanosheets

In a chemical synthesis, a mixture of 6 mmol (2.119 g) $C_{15}H_{21}FeO_6$, 8 mmol (0.888 g) SeO_2 and 50 mL peha was mixed into a 250 mL four-neck flask. Under an argon flow, the mixture was heated to 383 K and held at this temperature for 60 min to remove low boiling-point solvents and oxygen. Then, the temperature was raised to 575 K at a heating rate of 0.06 K min^{-1} and maintained at this temperature for 180 min. At room temperature, a mixture of 1 mmol $C_{15}H_{21}FeO_6$ and 20 mL peha was injected into the reaction system. The mixed reaction solution was heated to 383 K at a heating rate of 4 K again and held at this temperature for 60 min. Finally, the temperature was raised to 453 K at a rate of 0.06 K min^{-1} and maintained at this temperature for 540 min. Reaction flow for the synthesis of $Fe_{14}Se_{16}(peha)_{0.7}$ nanosheets is plotted in Fig. S2. A precipitate was separated by centrifugation at room temperature. An inductively coupled plasma (ICP) analysis shows 0.212 mg mL^{-1} for Fe and 0.224 mg mL^{-1} for Se left in the supernatant, revealing that Fe and Se atoms come from the reactants that have been well-reacted to form the precipitate. The precipitate was rewashed by a mixture consisting of 30 mL of acetone and 5 mL of isopropanol three times. The dried precipitate was kept in a glovebox for characterization.

2.3. Materials characterization

Powder X-ray diffraction (XRD) pattern was recorded by using a D/Max-2400 diffractometer equipped with a Cu K_α radiation source at room temperature at a slow scanning rate of 1° min^{-1} in 0.01° steps. Le Bail refinement of FullProf software was used to solve the crystal structure. Fourier transform infrared (FT-IR) spectrum was recorded on a Nicolet iN10 MX & iS10 spectrometer using the KBr pellet technique. Morphology of the product was observed by a JSM 6301F and Thermo Scientific Apreo 2C field-emission scanning electron microscopy (FESEM) system. Elemental composition of the product was analyzed by Oxford energy dispersive X-ray (EDX) and ThermoFisher ICP spectroscopies. Transmission electron microscopy (TEM) images and selected area electron diffraction (SAED) patterns were recorded on a Tecnai G2

F20 microscope operated at an acceleration voltage of 200 kV. The specimen was prepared by evaporating a drop of dilute solution of hybrids dispersed in acetone on an amorphous carbon-copper grid. Thermal gravimetric analysis and differential scanning calorimetry (DSC) were carried out on a STA6000 thermal analyzer with a heating rate of 10 K min^{-1} between 300 and 800 K. The Bruker D8 advance diffractometer with molybdenum (Mo) heater was used to obtain in-situ high-temperature XRD patterns between 300 and 750 K in a vacuum. The Mo heater has been characterized by the peaks at 2θ = 40.56° and 58.61° corresponding to the (110) and (200) diffraction planes of Mo, respectively. In order to determine the valence state of Fe, soft Fe L-edge X-ray absorption (XAS) measurements were performed at BL08U1A of the Shanghai Synchrotron Radiation Facility (SSRF) in the total electron yield (TEY) mode at room temperature. Fe L-edge spectra consist of sharp peaks around 709 eV (L_3 edge) and 720 eV (L_2 edge), resulting from the spin-orbit splitting of the core levels. The background vacuum level was 1 × 10^{-9} Torr. The powder sample was pasted on a Cu conducting tape, and the angle between the incident synchrotron radiation and the tape was 90°. Scans were collected in 0.1 eV steps and 700–735 eV energy scale. X-ray photoelectron spectroscopy (XPS) was performed on a Thermo VG ESCALAB250 in order to determine the compositions of Fe ions. ^{57}Fe Mössbauer spectra were recorded by a conventional constant acceleration spectrometer operated in a multi-channel scaling mode at 5 K. The spectrometer was calibrated by a 25 μm thick natural abundance α-Fe foil. The isomer shifts were determined relative to that of α-Fe. The fitting was performed by the least squares method in the MossWinn software.

Optical absorption spectra were recorded on an Ultraviolet-visible (UV–vis) spectrophotometer (JASCO-550) in the diffuse reflectance mode with the $BaSO_4$ plate as a reference. Photoluminescence (PL) emission spectra (270 nm excitation) were measured by using a fluorescence spectrophotometer (Edinburgh Instruments, FLSP-920). The as-synthetic sample was pressed into a pellet by using a 1.2 GPa axial pressure with a steel die. Temperature dependence of resistivity of the sample pellet was studied by using a physical property measurement system (PPMS) in a DC four-probe method with silver contact in a temperature range of 300 and 55 K, below which temperature the resistance was out of the measurement range. Thermal transport behavior of the cold-pressed pellet was measured by using the PPMS at a zero magnetic field. DC magnetizations and hysteresis loops were recorded by using a vibrating sample magnetometer (VSM) in the PPMS equipped with a superconducting magnet with a maximum magnetic field of 140 kOe. The magnetic data were collected by using the standard mode in a temperature range of 5–300 K and by using the oven mode in a high vacuum state with a chamber pressure lower than 1 × 10^{-5} Torr between 300 and 750 K, respectively. Temperature dependence of AC susceptibility was investigated over a frequency range of 10^2–10^4 Hz in the PPMS. Photoinduced magnetization (PIM) effects were studied by introducing a green light (532 nm with a power of 15 mW) into a sample chamber of a quantum design superconducting quantum interference device (SQUID) magnetometer (MPMS-squid VSM-094) through a homemade magneto-optical rod with an optical fiber. The switching of light was controlled by an external switch.

3. Results and discussion

3.1. Chemical composition and structure analysis

An FESEM (Fig. 1(a)) image illustrates that the hybrid product possesses a nanosheet-shaped morphology with a thickness range of 100–300 nm and an edge length range of 1–8 μm. An EDX spectrum (inset of Fig. 1(a)) indicates the presence of Fe, Se, C and N, and Fe and Se are the only heavy elements in the nanosheet. The Au comes from Au films coating on the nanosheets. The relative molar ratio of Fe to Se was determined to be 46.24/53.76 (6.88/8) by EDX, very similar to an ICP result of 6.92/8 and a feed ratio of 7/8 (Table 1). It is further confirmed by a decomposition product (Figs. S3 and S4 and more details in Supplementary Information). Elemental mapping (Fig. 1(b–e)) shows even distributions of Fe, Se, C, and N in the hybrid product. An FT-IR spectrum (Fig. 1(f)) presents characteristic peaks of peha molecules featured by the vibration bands of $-CH_2-$, $-NH_2$, –NH– and –CN–. Similar to the Mn(peha) complexes previously reported [37], the band of δ–NH_2/ν–CN– shift from 1573/1035 cm^{-1} for the bending/stretching vibration of free peha molecules to 1608/1114 cm^{-1} for that of the hybrid nanosheets, revealing a formation of Fe(peha) complexes (Fig. S5). A molar ratio between inorganic Fe_7Se_8 and organic peha molecules is 2/0.7 for the hybrid nanosheets based on a thermal decomposition experiment (in Supplementary Information). A XPS spectrum of Fe 2p (Fig. 1(g)) reveals the existence of Fe^{3+} and Fe^{2+} in the hybrid nanosheets with a molar ratio of 1/2.4 (29.85 %/70.15 %) in a good agreement with Mössbauer fitting results below. The presence of Fe^{3+} and Fe^{2+} is also confirmed by XAS spectrum shown as the inset of Fig. 1(g). As a result, the hybrid nanosheets are a mixed-valence compound, similar to $Fe_3Se_4(en)_2$ (en = ethylenediamine) [29] and $Fe_{14}Se_{16}(tepa)_{0.8}$ [30], and a chemical formula is written as $Fe_{14}Se_{16}(peha)_{0.7}$ for the hybrid nanosheets.

Fig. 1(h) represents an XRD pattern of hybrid nanosheets collected at room temperature. All Bragg diffraction peaks obtained by a slow scanning process can be well indexed by the TEROR method using program Powder X [38], suggesting the same tetragonal crystal structure as that observed in a SAED (Fig. 2(b)). Two strong peaks at low 2θ angles of 9.12° and 18.29° are characterized to be (002) and (004) with lattice spacings of 9.67 and 4.84 Å, respectively. It reveals a periodic layered structure of $Fe_{14}Se_{16}(peha)_{0.7}$, similar to organic-inorganic hybrids with the space group $I4/m$ [30,39]. Based on a slow scanning powder XRD pattern, the crystal structure of $Fe_{14}Se_{16}(peha)_{0.7}$ was refined by Le Bail refinement using the Fullprof software [40,41]. The refinement process gives good R factors (R_p = 12.0 %, R_{wp} = 10.7 %, R_{exp} = 3.70 % and χ^2 = 8.3) for the space group $I4/m$. Room-temperature lattice parameters are determined to be 8.602(1) Å for a and 19.384(0) Å for c, respectively. The XRD peaks with corresponding indices of crystal face, 2θ angles, and refined interplanar spacings are listed in Table S1 (in Supplementary Information). With the atomic compositions, inorganic building units, organic complexes and the electrical neutrality principles, a possible chemical formula for the hybrid nanosheets is $(\beta - Fe^{2+}_{2.5}Fe^{3+}_{0.5}Se^{2-}_4)_4[Fe^{3+}(peha)]_{0.7}Fe^{3+}_{1.3}$, where proportions of Fe^{2+} and Fe^{3+} well agree with Mössbauer fits (Table S2). A structural sketch for $Fe_{14}Se_{16}(peha)_{0.7}$ is illustrated in Fig. 1(i).

Fig. 2(a) illustrates TEM image of a $Fe_{14}Se_{16}(peha)_{0.7}$ nanosheet. A corresponding SAED pattern in Fig. 2(b) reveals a periodic crystal structure along the c direction. Clear diffraction points in the SAED pattern reveal a single crystal feature of tetragonal hybrid nanosheets. The SAED pattern is identical to that of tetragonal β-Fe_3Se_4 along the [001] direction [24]. The c axis zone SAED pattern of β-Fe_3Se_4 is almost the same as that of the superconducting β-FeSe [42], except that the systematic absences in (h00), (0k0), h odd, k odd, are now visible. The points of intersection of red lines in Fig. 2(b) reveal the diffraction planes of (010), (100), (110), (020), (200), (220) for a β-Fe_3Se_4 superstructure. Similarly, a crystal structure dependence of host layer was also found in intercalated FeSe-derived superconductors [39]. We examine the tetragonal structure by rotating a hybrid nanosheet with angles of 29.15° for the α angle and 10.83° for the β angle illustrated as Fig. 2(c). It generates a tilted angle of ~30.7° against the original position of

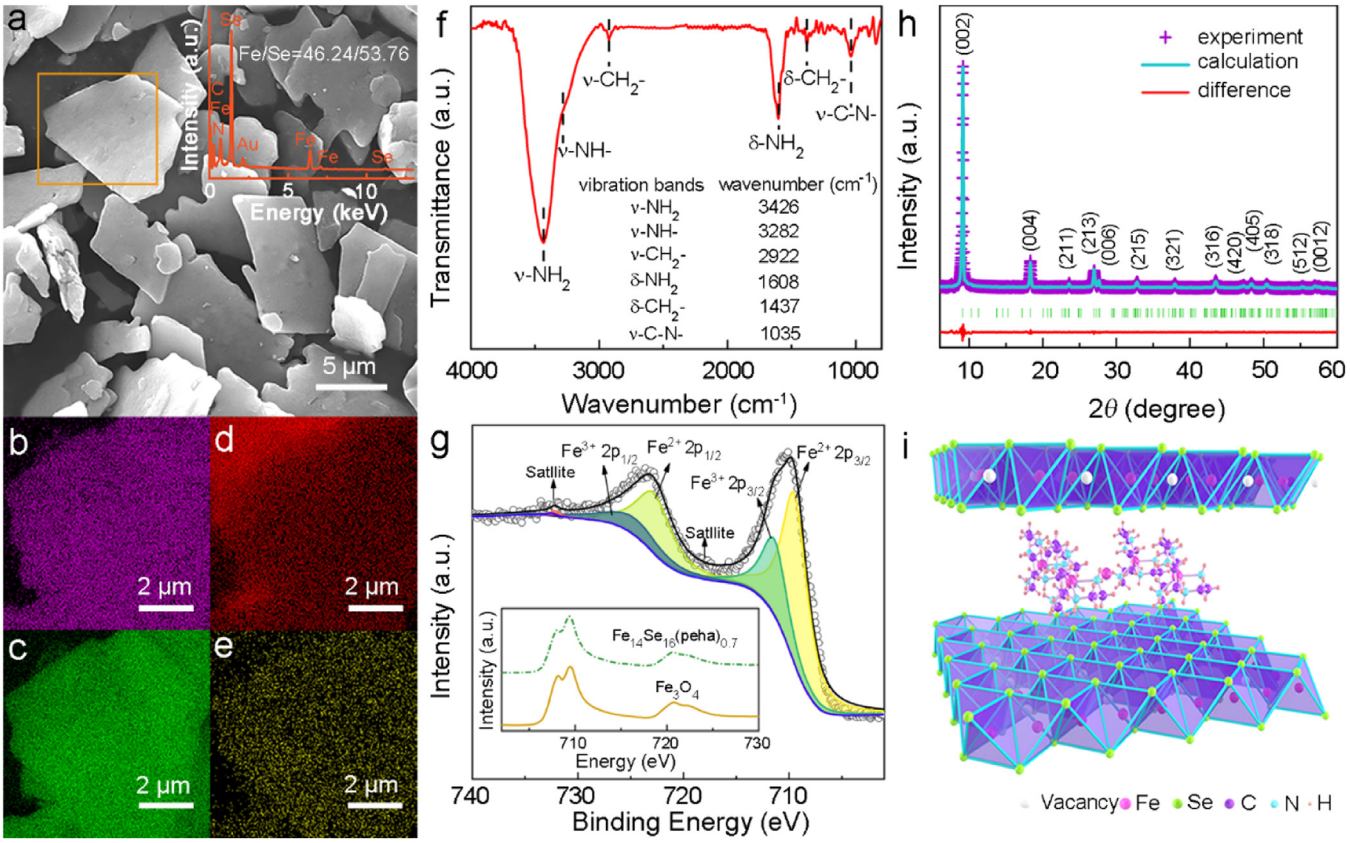

Fig. 1. Morphology, chemical compositions and phase of $Fe_{14}Se_{16}(peha)_{0.7}$ hybrid nanosheets. (a) FESEM image. The inset shows an EDX spectrum. Element mapping of (b) Fe, (c) Se, (d) C and (e) N for a hybrid nanosheet marked by a yellow box in (a). (f) FT-IR spectrum. (g) XPS spectrum of Fe 2p. The inset shows an Fe L-edge XAS with commercial Fe_3O_4 as a reference. (h) Slow scanning XRD pattern recorded at room temperature (solid crosses) with Le Bail refinement and difference curves. The vertical bars indicate the Bragg reflection positions. (i) A structural sketch of layered hybrid structure constructed by β-Fe_3Se_4 layers and spacer layers composed of iron ions and organic peha molecules.

Table 1
Compositions, semiconductor and magnetic properties of $Fe_{14}Se_{16}(peha)_{0.7}$.

Fe/Se			Fe_7Se_8/peha	E_g (eV)	E_a (meV)	M_S (emu g^{-1})			T_B (K)	T_f (K)	T_C (K)
Feed	ICP	EDS				5 K	300 K	500 K			
7:8	6.92:8	6.88:8	2:0.7	2.22	62.69	5.91	4.60	3.80	90	128.2	>519

the hybrid nanosheet (Fig. 2(a)). A corresponding SAED pattern of the tilted hybrid nanosheet (Fig. 2(d)) reveals a crystal zone axis of [$\bar{1}$11] following the Weiss zone law. To the rotation limit of the instrument, the experimental tilted angle is the same as the included angle of 31.8° between crystal zone axes of [001] and [$\bar{1}$11] according to a tetragonal symmetry. It suggests that the $Fe_{14}Se_{16}(peha)_{0.7}$ hybrid nanosheets are single crystals and well match the tetragonal crystal structure. However, we tried to grow single crystals sizable for single crystal diffraction but failed by prolonging reaction time because the growths of $Fe_{14}Se_{16}(peha)_{0.7}$ single crystals do not follow the Ostwald ripening mechanism (Fig. S6).

Effects of high temperatures on structure and phase are also studied to see if peha molecules can create an excellent thermal stability. A DSC curve in Fig. 3(a) shows an endothermic peak with an onset temperature (T_{onset}) of 519 K that emerges below the decomposition temperature (T_d ~600 K) (Fig. S3). Fig. 3(b) shows no obvious changes in terms of the peak intensity, position, and peak numbers of XRD patterns recorded between 300 and 500 K, indicating that the as-synthetic $Fe_{14}Se_{16}(peha)_{0.7}$ maintain the original lattice upon heating. As a measurement temperature rises to 550 K, a new XRD peak at $2\theta = 43.28°$ marked by the star symbol is observed in the XRD pattern. Above the T_d, thermal decomposition products of $Fe_{14}Se_{16}(peha)_{0.7}$ are indexed to Fe_3Se_4 and Fe_7Se_8. A slight amount of Fe_3O_4 is formed in the heating process. Thus, the $Fe_{14}Se_{16}(peha)_{0.7}$ is thermally stable below 519 K.

3.2. Semiconducting properties and thermal transport

UV–vis diffuse reflection spectrum in Fig. S7 shows that $Fe_{14}Se_{16}(peha)_{0.7}$ nanosheets absorb broad visible light. The absorbance gradually becomes weak as the wavelength changes from the blue light to the red light. Tauc plot using diffuse reflectance data with $(\alpha h\nu)^{1/n} = B(h\nu - E_g)$ ($n = 1/2$) in Fig. 4(a) gives a direct optical bandgap (E_g) of 2.22 eV, where α represents absorption coefficient, h the Planck-constant and ν frequency of a semiconductor. The band gap is similar to that (2.1 eV) of hybrid semiconductor thin films of bismuth based perovskites for solar cell [43]. A tail-like structure below the bandgap in the optical absorption spectrum is similar to that of Cu_2O nanowires [44]. PL emission spectrum of $Fe_{14}Se_{16}(peha)_{0.7}$ is contributed by two photo responses in a wavelength range between 350 and 620 nm at 300 K (Fig. 4(b)). The emission peak shifts towards lower energy (~405 nm) as compared to the value for free peha molecules (431 nm), which is induced by a strong electron charge trans-

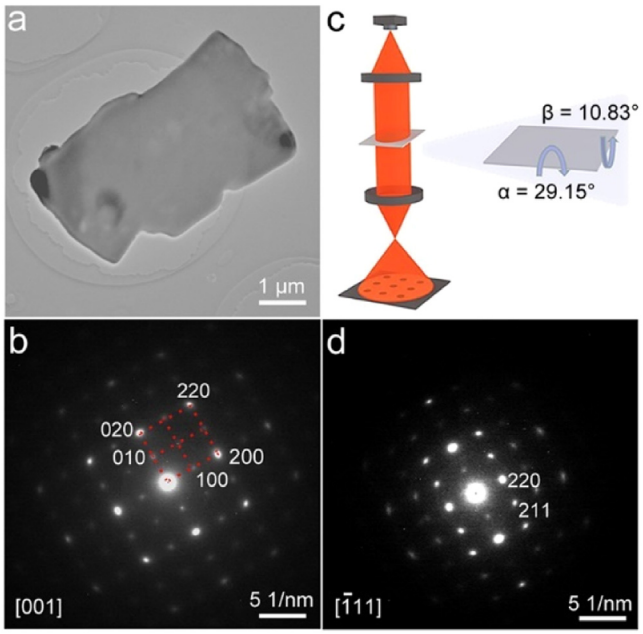

Fig. 2. (a) TEM image and (b) its corresponding SAED pattern of a $Fe_{14}Se_{16}(peha)_{0.7}$ hybrid nanosheet along the [001] direction. The points of intersection of the red lines in (b) indicate the diffraction planes of the (010), (100), (110), (020), (200), (220) of β-Fe_3Se_4 layers. (c) Schematic illustration for rotating a hybrid nanosheet in (a) from the [001] to the [$\bar{1}$11] with 29.15° for the α angle and 10.83° for the β angle. (d) SAED pattern of the hybrid nanosheet obtained along the [$\bar{1}$11] direction.

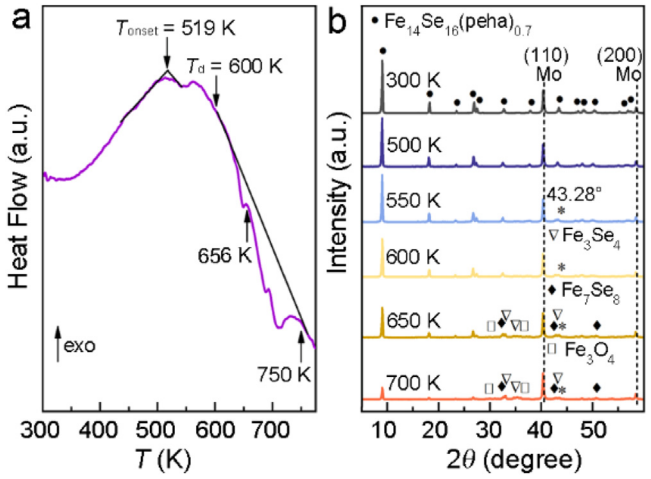

Fig. 3. (a) DSC curve and (b) in-situ high-temperature XRD patterns of the $Fe_{14}Se_{16}(peha)_{0.7}$ hybrid nanosheets. The star symbol * in (b) indicates a new XRD peak emerging from the as-synthetic $Fe_{14}Se_{16}(peha)_{0.7}$ in the heating process.

ferring from the coordinated iron ions towards organic molecules [30]. In contrast to free peha molecules, PL measurement on the nanosheets sample gives a broad peak with a maximum at ~550 nm, which corresponds to 2.25 eV, consistent with the band gap values obtained from UV–vis spectroscopy and diffuse reflectance.

Temperature dependence of electrical resistivity ρ on a logarithmic scale of a specimen pellet of $Fe_{14}Se_{16}(peha)_{0.7}$ is plotted in

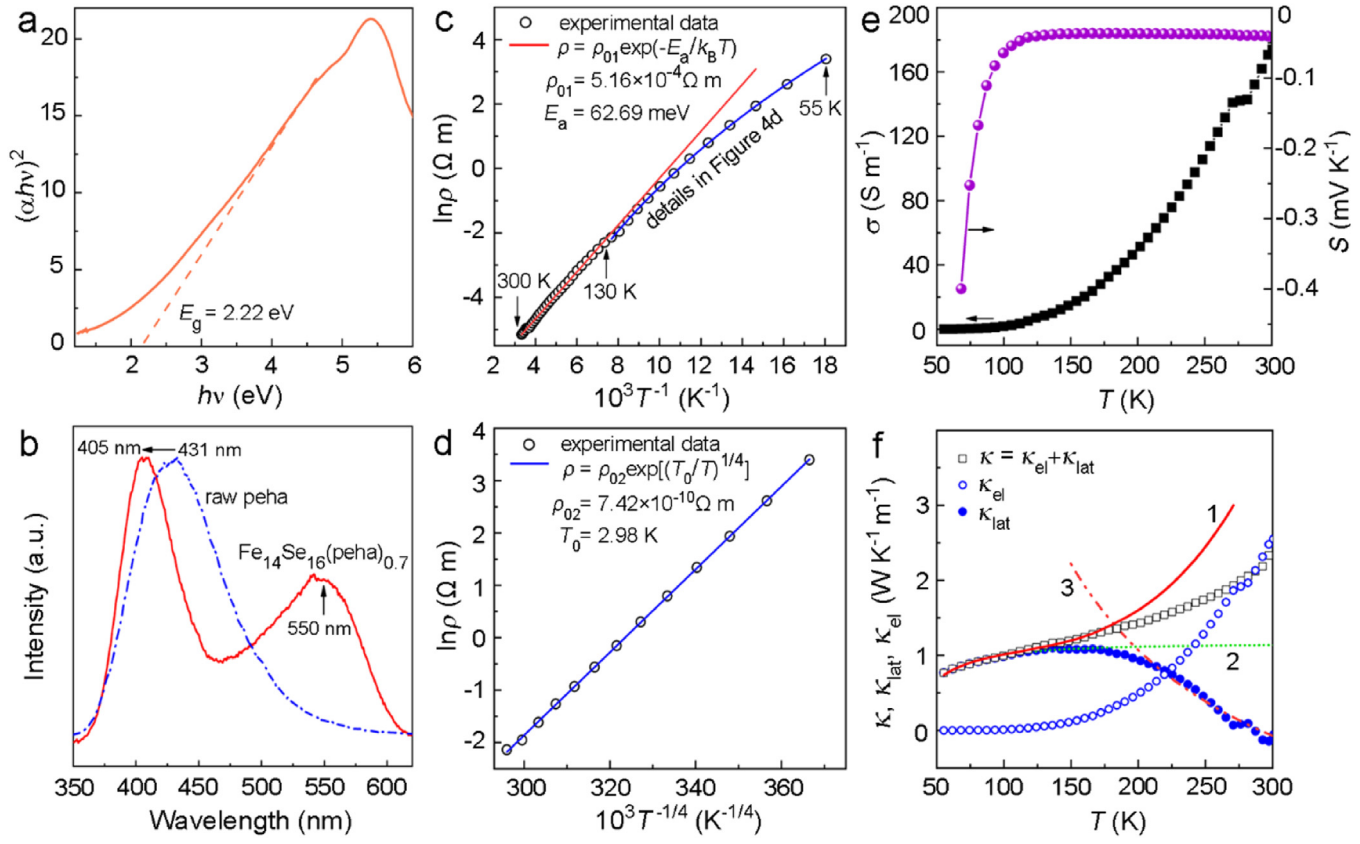

Fig. 4. Semiconducting properties of $Fe_{14}Se_{16}(peha)_{0.7}$ hybrid nanosheets. (a) Tauc plot for a direct allowed transition. (b) PL spectrum obtained with 270 nm excitation at 300 K. Plot of resistivity on a logarithmic scale against (c) T^{-1} over 55–300 K and (d) $T^{-1/4}$ over 55–130 K. The resistivity data (blank dots) are recorded by using a current of 10 μA, while the solid lines indicate the linearity of data. (e) Temperature dependence of electrical conductivity (σ) and Seebeck coefficient (S). (f) Temperature dependence of thermal conductivity (κ), the calculated electron (κ_{el}) and phonon (κ_{lat}) contributions. Lines 1–3 are the fit curves as described in the main text.

Fig. 4(c). The ρ at 300 K is 5.8 × 10^{-3} Ω m and resistance data below 55 K, which are beyond the measurement range, were not given. A good linear relation is seen between lnρ and inverse temperature (T^{-1}) in the 130–300 K range, showing a typical semiconducting feature of thermally-activated electrical conduction. Based on the Arrhenius equation $\rho = \rho_{01}e^{-E_a/k_BT}$, where ρ_{01} is a constant, an E_a is extracted to be 62.69 meV. It is the energy separation between the bottom of the conduction band and an impurity energy level within the intrinsic bandgap, or the energy barrier for a charge transfer between the spacer layers and the inorganic host layers by means of the Se...H–N interactions [30,45]. Obviously, lnρ against T^{-1} in the 55–130 K range deviates from the linear relation. Instead, Fig. 4(d) represents a satisfactory linear fit of lnρ against $T^{-1/4}$ in a temperature region from 55 K to 130 K. The VRH conductivity in a 3D case follows $\rho = \rho_{02}\exp[(T_0/T)^{1/4}]$ that was derived by Mott [46], where ρ_{02} is a material constant and T_0 is the characteristic temperature of the system, revealing that charge carriers are localized over the transport sites by disorder in $Fe_{14}Se_{16}$(peha)$_{0.7}$. A VRH conduction behavior is dominated by a degree of disorder in a material whether it is a metal or a semiconductor [47]. Previously, intercalations of metal (Tl, K, Rb, Cs) atoms into adjacent AFM β-Fe_3Se_4 layers produced a series of quasi-2D AFM semiconductors with energy band gaps of 94, 121, 69, and 26 meV for $TlFe_{1.5}Se_2$, $KFe_{1.5}Se_2$, $RbFe_{1.5}Se_2$, and $CsFe_{1.5}Se_2$, respectively [48], while Fe^{2+}(tepa) complexes and uncoordinated Fe^{2+} served as spacer layers result in VRH-type $Fe_{14}Se_{16}$(tepa) and $Fe_{14}Se_{16}$(tepa)$_{0.8}$ at 300 K [30]. Therefore, tunability of the electronic structure in Fe^{3+}/peha co-intercalated β-Fe_3Se_4 leads to a band gap of 2.22 eV for $Fe_{14}Se_{16}$(peha)$_{0.7}$. Temperature-dependent Seebeck coefficient (S) in Fig. 4(e) is consistent with the electrical transport results. Negative signs of S indicate a n-type semiconductor of $Fe_{14}Se_{16}$(peha)$_{0.7}$ [49]. The S reaches a maximum at a temperature when the derivative of electrical conductivity (σ) diverges, well described by the VRH conduction [47].

Understanding the thermal conductivity of organic magnetic semiconductors is key to optimizing organic spintronic devices [50]. Temperature dependence of thermal conductivity of $Fe_{14}Se_{16}$(peha)$_{0.7}$ is given in Fig. 4(f). The $Fe_{14}Se_{16}$(peha)$_{0.7}$ possesses considerably low κ values of about 0.8–2.5 W m^{-1} K^{-1} in the temperature range of interest. Such low values may be attributed mainly to the soft modes or strong anharmonicity due to the weak interaction between the inorganic β-Fe_3Se_4 host layers and space layers consisting of organic peha molecules and Fe ions, just similar to the iron sulfide hybrid semiconductor that is featured by a low band gap due to unique 2D $[Fe_{16}S_{20}]^{8-}$ layers [51].

It is essential to separate the contributions to the total thermal conductivity by both electron and lattice. To note that κ_{lat}, which is very low at 55 K, can be further suppressed by temperature due to the Umklapp process. Meanwhile, total κ goes up with temperature, indicating that thermal conductivity is dominated by κ_{el} at relatively high temperatures and therefore we may assume that κ_{lat} drops to zero at 300 K. Taking κ as κ_{el} at 300 K, we can resort to the W-F law ($\kappa_{el} = \sigma L_0 T$) to obtain temperature dependence of κ_{el} in the whole temperature range of interest. However, for organic semiconductor systems, the violation of the W-F law is quite common due to decoupling the charge conductivity and thermal conductivity and the κ_{el} is usually ruled by a modified W-F law (Eq. (1)):

$$\kappa_{el} = \sigma LT \tag{1}$$

The $\kappa_{el}(T)$ obtained is shown by blue empty dots in Fig. 4(f).

The VRH conduction strongly localizes electrons in the 55–130 K range, limiting the electronic thermal conductivity. Therefore, the lattice counterpart takes over, for example at 55 K, the κ_{lat} is ~0.8 W m^{-1} K^{-1} and κ_{el} almost negligible to the κ, which is reasonable because the electrical transport is not diffusive anymore below 130 K. With $\kappa_{el}(T)$ at hand, it is straightforward to get $\kappa_{lat}(T)$, as given by blue filled dots in Fig. 4(f). In the 55–130 K range, κ_{lat} increases with temperature and shall be ballistic type. In the ballistic thermal transport scenario, the κ_{lat} can be described by $C_v\upsilon D$, in which C_v, υ, and D are specific heat, phonon velocity and sample size, respectively. Considering both υ and L are usually temperature independent, we can evaluate κ_{lat} based on the temperature dependence of specific heat C_v by the Einstein model (Eq. (2)),

$$\kappa_{lat} = 3\frac{R\upsilon D}{\pi}\left(\frac{\Theta_E}{T}\right)^2\frac{e^{\Theta_E/T}}{\left(e^{\Theta_E/T}-1\right)^2} \tag{2}$$

where Θ_E is the Einstein temperature and R is the gas constant [52]. The fit shown as the red line 1 in Fig. 4(f) is satisfactory with the experimental κ between ~55 and 130 K, which gives a Lorenz number L (~2000L_0) and the Θ_E of 131 K. Hopping conduction induces a significant reduction of the electrical conductivity below 130 K, whereas the transport of heat, through lattice vibrations, can remain high, leading to an enhancement in L/L_0 [21]. Thus, the green fit line 2 further illustrates that the lattice contribution κ_{lat} below 130 K is dominated by the Einstein model. In the 250–300 K temperature range, the phonon transport is well described by the phonon-phonon Umklapp processes (κ_{lat} ~$1/T$) (red dotted line 3) [53]. Thus, the κ_{el} dominates the thermal conductivity of $Fe_{14}Se_{16}$(peha)$_{0.7}$ above 250 K.

3.3. Magnetic performance

Fig. 5(a) presents the zero-field-cooled (ZFC)/field-cooled (FC) magnetization curves and temperature dependence of AC susceptibilities of $Fe_{14}Se_{16}$(peha)$_{0.7}$ measured in the 5–300 K range in a zero field. The FC magnetization smoothly decreases with raising the temperature from 5 K to 300 K, but there is a broad peak from 2 K to ~100 K in the ZFC magnetization curve recorded at a magnetic field of 0.1 kOe. A peak temperature (~90 K) of the ZFC magnetization peak is obviously lower than an AC susceptibility peak at ~128.2 K measured at a frequency of 0.1 kHz. The inset of Fig. 5(a) shows a shift of AC susceptibility peak from 121.1 K to 136.0 K with increasing frequency from 1 kHz to 10 kHz. It reveals a spin-glass behavior with a freezing temperature (T_f) of 128.2 K within the hybrid system [54]. A field (H) dependence of magnetization (M) in Fig. 5(b) exhibits strong ferrimagnetism of $Fe_{14}Se_{16}$(peha)$_{0.7}$ in the 5–500 K range. The M_S is 5.91 emu g^{-1} at 5 K, which gradually decreases to 4.6 emu g^{-1} at 300 K and 3.8 emu g^{-1} at 500 K, respectively, while a coercivity (H_C) of $Fe_{14}Se_{16}$(peha)$_{0.7}$ is 0.42 kOe at 5 K but ~0 at 300 and 500 K. A big M_S value but a zero H_C of $Fe_{14}Se_{16}$(peha)$_{0.7}$ at 300 K reveals a superparamagnetic behavior, supported by nonmagnetic doublets of ^{57}Fe Mössbauer spectrum of $Fe_{14}Se_{16}$(peha)$_{0.7}$ collected at 300 K in Fig. 5(d). This feature is also observed in a spectrum recorded at 100 K (Fig. 5(e)), suggesting that the broad peak in the ZFC magnetization curve well matches to the superparamagnetic components with the maximum blocking temperature (T_B) of ~90 K. A peak on the ZFC magnetization curve (Fig. 5(a)) indicates a wide distribution of T_B values, which are related to sizes of magnetic nanoparticles [55]. When the anisotropy energy barrier is higher than thermal energy, thermal fluctuations will be overcome below a T_B. As a result, nonmagnetic doublets become weak and magnetically splitting sextets emerge on a spectrum recorded at 5 K (Fig. 5(d)). It further reveals the presence of long-range FIM ordering in $Fe_{14}Se_{16}$(peha)$_{0.7}$, identical to the saturation magnetization behaviors of M–H loops in Fig. 5(b). Spin frustrations usually occur on boundaries and/or interfaces of hybrid nanosheets. Electron spin resonance spectra reveal that spin-glass components and ferrimagnetic components can well coexist in hybrid materi-

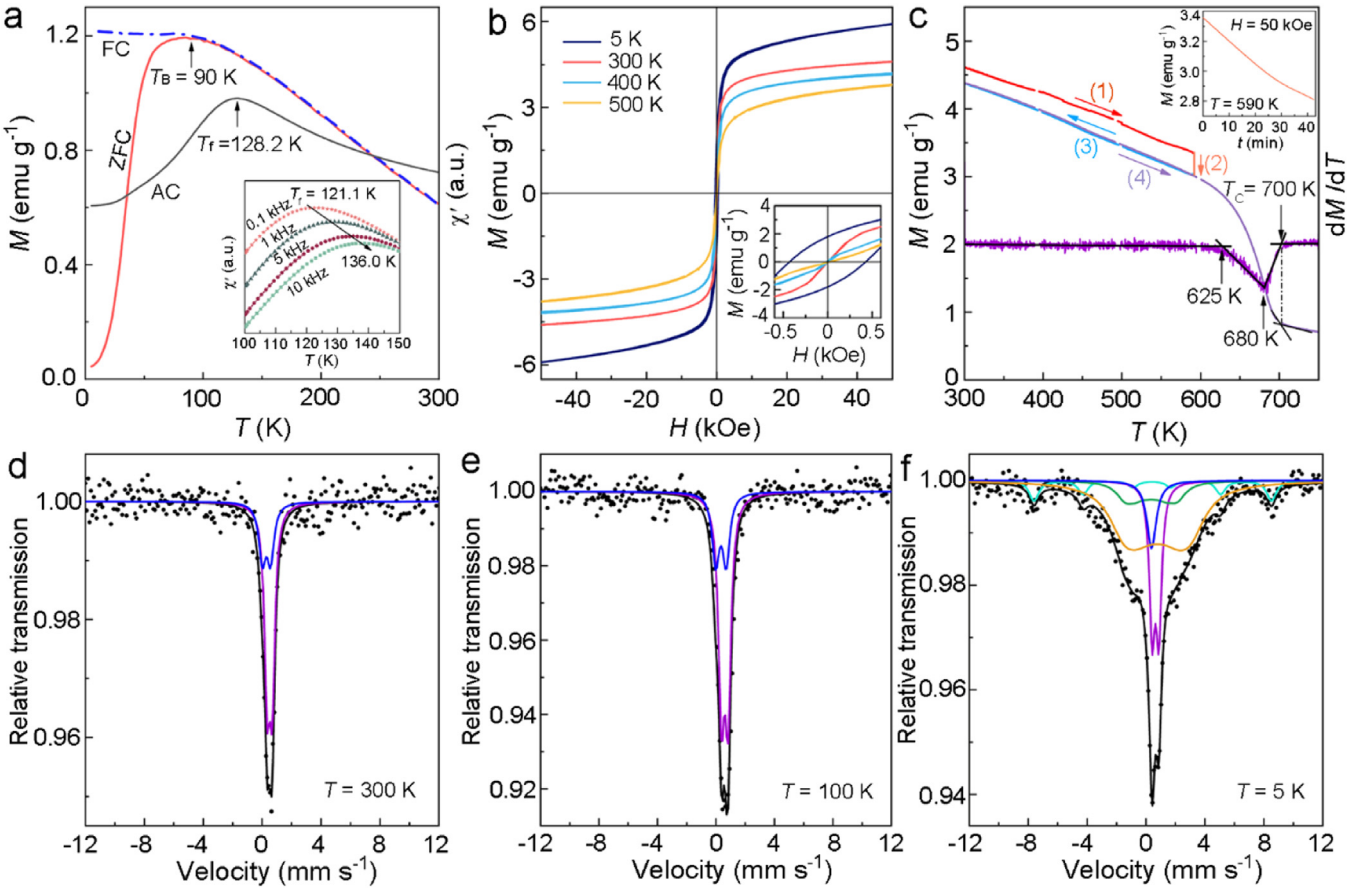

Fig. 5. Magnetic properties and Mössbauer spectra of $Fe_{14}Se_{16}(peha)_{0.7}$ semiconductor. (a) Temperature dependence of ZFC and FC magnetizations recorded at a magnetic field (H = 0.1 kOe) and AC susceptibilities measured in the 5–300 K range at zero magnetic field. The inset shows a frequency dependence of AC susceptibility. (b) Hysteresis loops measured at different temperatures. The inset shows the details in a low magnetic field range. (c) Temperature dependence of magnetization and dM/dT curves in a series of warming or cooling processes from 300 K to 750 K at a magnetic field of 50 kOe. Mössbauer spectra recorded at (d) 300 K, (e) 100 K and (f) 5 K. Experimental data (black dot) and calculated spectrum (black line) fitted by Fe^{3+} components [cyan (S = 5/2) and green (S = 1/2) for magnetically splitting sextets, blue (S = 1/2) for doublets] and Fe^{2+} components [yellow (S = 2) for magnetically splitting sextets and purple (S = 1) for doublets]. The spin states of irons are shown in the brackets, while the different colored lines represent nonequivalent sites of Fe^{2+} and Fe^{3+} in the hybrid.

als because two components are dependent on different structural motifs of $Fe_{14}Se_{16}(peha)_{0.7}$ [25,27]. No magnetic transition on the FC magnetization curve (Fig. 5(a)) indicates that the T_C of the organic magnetic semiconductor is higher than room temperature. This conclusion is supported by high-temperature thermal magnetization curves and a dM/dT curve (Fig. 5(c)). The magnetization of $Fe_{14}Se_{16}(peha)_{0.7}$ smoothly decreases with raising a temperature from 300 K to 590 K (process 1). When the temperature is maintained at 590 K for 40 min (process 2), the magnetization slightly decreases with prolonging the measurement time due to a change of the hybrid structure at high temperatures (an inset of Fig. 5(c)). According to smooth M-T curves in the 300–590 K range, there are no FIM impurities of Fe_3Se_4 (T_C ~ 332 K) and Fe_7Se_8 (T_C ~ 453 K) in our magnetic semiconductor [25]. An obvious magnetization drop in a warming process (4) starts at ~ 625 K and the fastest decrease of magnetization occurs at ~680 K corresponding to decomposition. A magnetization change almost completes at ~700 K, which is determined by the point of intersection of the two tangents around the inflection point of the warming M-T curve. Such a temperature is much lower than the T_C of Fe_3O_4 (~860 K), excluding an effect of impure Fe_3O_4 on the magnetic properties of $Fe_{14}Se_{16}(peha)_{0.7}$. XPS data (Fig. 1(g)) reveal the binding energy of 709.5 and 711.4 eV for Fe^{2+} $2p_{3/2}$ and Fe^{3+} $2p_{3/2}$ in the hybrid semiconductor, respectively, which exclude impurities Fe_3O_4 and Fe due to different binding energy of 710.4 eV for $Fe2p_{3/2}$ in Fe_3O_4 and 706.8 eV for $Fe2p_{3/2}$ of Fe. Therefore, the T_C (>519 K) and room-temperature M_S of as-synthetic $Fe_{14}Se_{16}(peha)_{0.7}$ are indisputably higher than not only the previously calculated magnetic ordering temperatures [18,56,57] but also the experimental values [14–17,20,33–36,58–61] (Fig. 6). Such an unusual high T_C of $Fe_{14}Se_{16}(peha)_{0.7}$ is never reported in inorganic 2D magnetic semiconductors, such as $Cr_2Ge_2Te_6$ (T_C = 64 K) [6], FeTe (T_C = 220 K) [62] and $CoFe_2O_4$ (T_C = 390 K) [10].

Mössbauer spectroscopy is an effective tool to determine the magnetic ground state of a magnetic material, especially for the distribution, valence and spin states of irons. According to Fig. 5(d, e), two nonmagnetic doublets are well-fitted for Fe^{2+} and Fe^{3+} and the fit parameters are summarized in Table S2. Slight increases in isomer shift (IS) and quadrupole splitting (QS) are induced by cooling a temperature from 300 K to 100 K. The Fe^{3+} may have three spin states: S = 1/2, 3/2, and 5/2, which are much different from the spin states of S = 0, 1, and 2 for the Fe^{2+}. Usually, IS values (>0.6 mm s^{-1}) are expected to Fe^{2+}, and smaller IS values (0.27–0.39 mm s^{-1}) are for Fe^{3+} [29,63]. The IS values in 0.3–0.5 mm s^{-1} and 0.6–0.8 mm s^{-1} at 5 K confirm the presence of Fe^{3+} and Fe^{2+} in the hybrid, respectively. Thus, the $Fe_{14}Se_{16}(peha)_{0.7}$ is a mixed-valence compound containing well-separated Fe^{2+} (S = 1) and Fe^{3+} (S = 1/2) sublattices. The proportions for Fe^{3+} (blue) and Fe^{2+} (purple) are 28.6 % and 71.4 %, respectively, which is consistent with the XPS result (Fig. 1(g)). Besides nonmagnetic doublets, magnetically splitting sextets can be obviously observed on a spectrum recorded at 5 K (Fig. 5(f)). Previously, magnetically

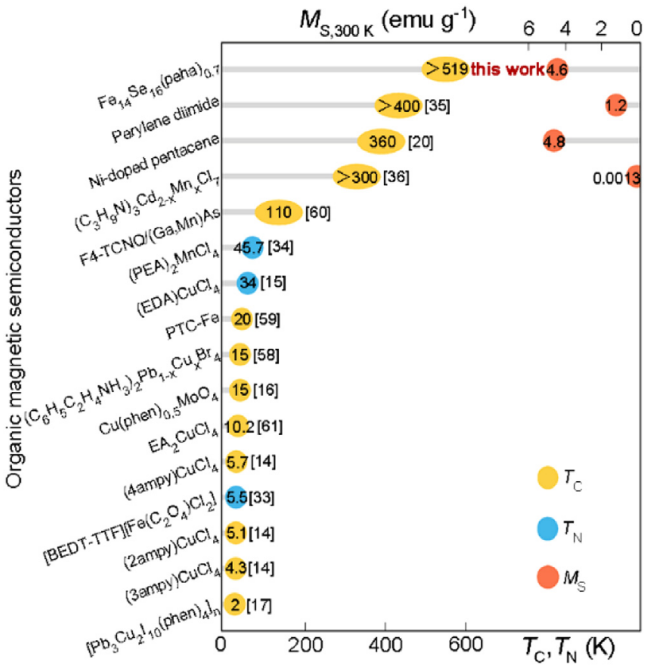

Fig. 6. Comparison of magnetic ordering temperatures and saturation magnetizations of $Fe_{14}Se_{16}(peha)_{0.7}$ and some reported inorganic/organic magnetic semiconductors in experiments.

nonequivalent sites of high-spin Fe^{3+} with hyperfine fields of 507 and 468 kOe and Fe^{2+} with hyperfine fields of 272 and 231 kOe [30] were found in inorganic β-Fe_3Se_4 layers due to ordered Fe vacancies (Fig. S8). In the present case, superparamagnetic components give rise hard to identify sites of magnetic Fe ions in the hybrid lattice. Thus, we assume only one high-spin Fe^{3+} component and one high-spin Fe^{2+} component in the presence of inorganic β-Fe_3Se_4 layers, while signals of nonmagnetic irons are from superparamagnetic nanosheets. Magnetic irons in spacer layers can be assigned to the third magnetically splitting sextet [30,64]. Therefore, a hyperfine field of 501 kOe for high-spin Fe^{3+} (cyan) at 5 K is significantly higher than an expected value of ~257 kOe for $S = 3/2$ but close to the typical value of ~500 kOe for Fe^{3+} ($S = 5/2$) [63]. A magnetically splitting sextet (green) exhibits an HF of 110 kOe, which is about twice that (66 kOe) of Fe^{2+} ($S = 2$) in $[Fe^{2+}(en)_2]$ complexes [29]. An IS value of 0.33 mm s^{-1} assigns the green component to low-spin Fe^{3+} in organic Fe^{3+}(peha) complexes. An IS value of 0.76 mm s^{-1} indicates a high-spin Fe^{2+} component of magnetically splitting sextet (yellow) with an HF of 141 kOe, which is lower than the HF value for Fe^{2+} ($S = 2$) [30]. The magnetically splitting sextets and high hyperfine fields of high-spin Fe^{3+} (cyan) and Fe^{2+} (yellow) at 5 K confirm the presence of long-range magnetic ordering in the $Fe_{14}Se_{16}(peha)_{0.7}$. In contrast to Fe/$NH_3$ co-intercalated $(NH_3)Fe_{0.25}Fe_2S_2$ [64] and Fe/tepa co-intercalated $(Fe^{2+}_{2.5}Fe^{3+}_{0.5}Se^{2-}_4)_4[Fe^{3+}(tepa)]Fe^{3+}$ [31], a 3D long-range AFM interaction between interlayer and intralayer irons with various HF values is responsible for ferrimagnetism of $Fe_{14}Se_{16}(peha)_{0.7}$.

Distinguishing features of $Fe_{14}Se_{16}(peha)_{0.7}$ are commented on in the following. The XRD and SAED patterns indicate a layered single-crystalline structure. The UV–vis diffuse reflection/PL emission spectra, electrical conduction and Seebeck coefficient data clarify an n-type semiconducting behavior, while the hysteresis loops and ZFC/FC magnetization curves strongly support the room-temperature ferrimagnetism of this organic semiconductor. A single phase indicates that our bottom-up self-assemble strategy is an effective method to exploit room-temperature organic magnetic semiconductors. In our present case, physical properties on semiconducting and FIM properties are observed in layered organic-inorganic hybrid nanosheets with β-Fe_3Se_4 layers separated by spacer layers containing Fe and peha. It is sure that varied chemical compositions and hybrid structures can result in significant changes in magnetic and electrical performance on a similar hybrid system [30]. Thus, an intrinsic FIM semiconductor of $Fe_{14}Se_{16}(peha)_{0.7}$ with a T_C higher than 519 K was successfully synthesized. The thermal conductivity of $Fe_{14}Se_{16}(peha)_{0.7}$ at 300 K is only twice that of SiO_2. It not only offers an appropriate system for the investigation of thermal properties on organic magnetic semiconductors, but also suggests a potential integration of this organic FIM semiconductor with silicon-based semiconductor materials. The σ in the 130–300 K temperature range is in the magnitude of 170–180 S m^{-1}. However, high-temperature superconductivity induced by co-intercalations of Na^+/en in β-FeSe [39] and Fe^{2+}/tepa in β-Fe_3Se_4 [30] indicates tunability of different metal ions and amine molecules as well as iron vacancies on electronic structures in this room-temperature FIM semiconductor system. A high conductivity is worth pursuing in an organic magnetic semiconductor before it can be applied to spintronics. Although the W-F law is strongly violated according to the electrical-thermal transport data, it is important that organic spintronic devices require proper heat dissipation capability to utilize/prevent heat accumulation for device high performance [65].

Moreover, high absorbance (>0.75) in the visible light range (Fig. S7) makes the $Fe_{14}Se_{16}(peha)_{0.7}$ attract much attention in the optical control of magnetism in magnetic semiconductors [66]. A PIM effect is expected by possible change of spin configurations from low-spin (LS) $Fe^{II,LS}$ to $Fe^{III,LS}$ (Fig. S9(a)) or from intermediate-spin (MS) $Fe^{III,MS}$ to high-spin (HS) $Fe^{III,HS}$ (Fig. S9(b)) due to light-induced electron transfers. However, Fig. S9(c, d) shows weak PIM effects. Mössbauer spectrum in Fig. 5 reveals varied spin states of Fe^{2+} and Fe^{3+} in $Fe_{14}Se_{16}(peha)_{0.7}$. However, the spin states of Fe^{2+} ($S = 1$ and 2) and Fe^{3+} ($S = 1/2$ and 5/2) in $Fe_{14}Se_{16}(peha)_{0.7}$ do not meet the light-induced electron transfers. Nevertheless, it is fascinating to systematically study a structure-performance relationship of room-temperature organic magnetic semiconductors with various spin states of irons due to varied crystal symmetries, organic/inorganic components, and so on [29,30,63]. Efforts to examine correlations between oxidation/spin states of irons and semiconducting/optical/magnetic properties of this system are currently in progress.

4. Conclusion

In summary, we report a tetragonal 2D organic-inorganic hybrid FIM semiconductor of $Fe_{14}Se_{16}(peha)_{0.7}$ with an unprecedented room-temperature ferrimagnetism and a T_C value higher than 519 K. The E_a and E_g of this n-type semiconductor are 62.69 meV and 2.22 eV, respectively. The W-F law is strongly violated in this organic FIM semiconductor, while the lower thermal conductivity (0.8–2.5 W m^{-1} K^{-1}) is attributed to the incorporation of organic peha molecules and Fe ions between β-Fe_3Se_4 host layers. Our discovery highlights a better understanding of the origin of magnetism and semiconducting performance in room-temperature hybrid FIM semiconductors for spintronic applications in the future.

Declaration of competing interest

The authors declare that they have no known competing financial interests or personal relationships that could have appeared to influence the work reported in this paper.

CRediT authorship contribution statement

Xiaoling Men: Writing – original draft, Methodology, Investigation, Data curation. **Fei Qin:** Investigation. **Bo Zhang:** Methodology. **Kangkang Yao:** Investigation. **Yin Zhang:** Writing – original draft, Methodology. **Yangtao Zhou:** Investigation. **Qifeng Kuang:** Investigation. **Xiaolei Shang:** Visualization. **Ruiqi Huang:** Data curation. **Zhiwei Li:** Methodology. **Sen Yang:** Methodology. **Gang Liu:** Writing – review & editing, Resources. **Teng Yang:** Writing – review & editing. **Da Li:** Writing – review & editing, Supervision, Conceptualization. **Zhidong Zhang:** Writing – review & editing, Supervision.

Acknowledgments

This work was financially supported by the National Natural Science Foundation of China (Nos. 52371203, 51971221 and 52031014). We also thank BL08U1A of the Shanghai Synchrotron Radiation Facility (SSRF).

Supplementary materials

Supplementary material associated with this article can be found, in the online version, at doi:10.1016/j.jmst.2025.02.031.

References

[1] S.A. Wolf, D.D. Awschalom, R.A. Buhrman, J.M. Daughton, S. von Molnar, M.L. Roukes, A.Y. Chtchelkanova, D.M. Treger, Science 294 (2001) 1488.
[2] H. Ohno, D. Chiba, F. Matsukura, T. Omiya, E. Abe, T. Dietl, Y. Ohno, K. Ohtani, Nature 408 (2000) 944.
[3] T.P. Chen, J.X. Lin, C.C. Lin, C.Y. Lin, W.C. Ke, D.Y. Wang, H.S. Hsu, C.C. Chen, C.W. Chen, ACS Appl. Mater. Interfaces 13 (2021) 10279.
[4] H. Sen, J. Phys. C 21 (1988) 4497.
[5] J.M. Coey, M. Venkatesan, C.B. Fitzgerald, Nat. Mater. 4 (2005) 173.
[6] Z. Wang, T.Y. Zhang, M. Ding, B.J. Dong, Y.X. Li, M.L. Chen, X.X. Li, J.Q. Huang, H.W. Wang, X.T. Zhao, Y. Li, D. Li, C.K. Jia, L.D. Sun, H.H. Guo, Y. Ye, D.M. Sun, Y.S. Chen, T. Yang, J. Zhang, S.P. Ono, Z. Han, Z.D. Zhang, Nat. Nanotechnol. 13 (2018) 554.
[7] C. Huang, J. Guan, Q. Li, F. Wu, P. Jena, E. Kan, Phys. Rev. B 103 (2021) L140410.
[8] Y. Wen, Z.H. Liu, Y. Zhang, C.X. Xia, B.X. Zhai, X.H. Zhang, G.H. Zhai, C. Shen, P. He, R.Q. Cheng, L. Yin, Y.Y. Yao, M.G. Sendeku, Z.X. Wang, X.B. Ye, C.S. Liu, C. Jiang, C.X. Shan, Y.W. Long, J. He, Nano Lett. 20 (2020) 3130.
[9] D.X. Wu, Z.W. Zhuo, H.F. Lv, X.J. Wu, J. Phys. Chem. Lett. 12 (2021) 2905.
[10] R. Cheng, L. Yin, Y. Wen, B. Zhai, Y. Guo, Z. Zhang, W. Liao, W. Xiong, H. Wang, S. Yuan, J. Jiang, C. Liu, J. He, Nat. Commun. 13 (2022) 5241.
[11] X.Y. Huang, J. Li, J. Am. Chem. Soc. 129 (2007) 3157.
[12] M. Zhang, C. Shi, T.K. Zhang, M. Feng, L. Chang, W.T. Yao, S.H. Yu, Chem. Mater. 21 (2009) 5485.
[13] M.A. Tershansy, A.M. Goforth, L. Peterson, M.C. Burns, M.D. Smith, H.Z. Loye, Solid State Sci. 9 (2007) 895.
[14] B. Sun, Z. Yan, Y. Cao, S.S. Ding, R.J. Li, B. Ma, X.Y. Li, H. Yang, W. Yin, Y.M. Zhang, Q. Wang, X.F. Shao, D.Z. Yang, D.S. Xue, H.L. Zhang, Adv. Mater. 35 (2023) e2303945.
[15] S. Dutta, D.S.K. Vishnu, S. Som, R. Chaurasiya, D.K. Patel, K. Moovendaran, C.C. Lin, C.W. Chen, R. Sankar, ACS Appl. Electron. Mater. 4 (2022) 521.
[16] Islah-u-din, S.V. Chong, G.B. Jamesonb, S.G. Raymonde, G. Leef, I.K. Park, X.I. Wang, M.R. Waterlandb, J.L. Tallon, J. Magn. Magn. Mater. 508 (2020) 166881.
[17] L.Q. Fan, X. Jin, D.X. Li, C.B. Tian, J.H. Wu, Dalton Trans. 46 (2017) 14738.
[18] X.X. Li, J.L. Yang, J. Am. Chem. Soc. 141 (2019) 109.
[19] Y. Zhang, L. Guo, X. Zhu, X. Sun, Front. Chem. 8 (2020) 589207.
[20] W.Y. Chou, S.K. Peng, F.H. Chang, H.L. Cheng, J.J. Ruan, T.Y. Ho, ACS Appl. Mater. Interfaces 13 (2021) 34962.
[21] N. Lu, L. Li, N. Gao, M. Liu, J. Appl. Phys. 120 (2016) 195108.
[22] D. Scheunemann, M. Kemerink, Phys. Rev. B 101 (2020) 075206.
[23] V. Sharma, G.S. Okram, Y.K. Kuo, Nanotechnology 34 (2022) 035702.
[24] T.K. Chen, C.C. Chang, H.H. Chang, A.H. Fang, C.H. Wang, W.H. Chao, C.M. Tseng, Y.C. Lee, Y.R. Wu, M.H. Wen, H.Y. Tang, F.R. Chen, M.J. Wang, M.K. Wu, D. Van Dyck, Proc. Natl. Acad. Sci. U. S. A. 111 (2014) 63.
[25] D.S. Pan, Y. Li, Z. Han, B. Li, C.W. Wang, T. Yang, D. Li, C.J. Choi, Z.D. Zhang, Chem. Mater. 30 (2018) 8975.
[26] Q.F. Kuang, X.L. Men, X.L. Shang, B. Yang, Y.T. Zhou, B. Zhang, Z.W. Li, D. Li, Z.D. Zhang, Magnetism 2 (2022) 31.
[27] D.S. Pan, Q.F. Kuang, P. Tong, W. Tong, L.B. Fan, J. Zhao, D. Li, C. Choi, Z.D. Zhang, J. Magn. Magn. Mater. 542 (2022) 16585.
[28] X.L. Shang, X.L. Men, Q.F. Kuang, S.J. Li, D. Li, Z.D. Zhang, Nanomaterials 13 (2023) 487.
[29] C. Pak, S. Kamali, J. Pham, K. Lee, J.T. Greenfield, K. Kovnir, J. Am. Chem. Soc. 135 (2013) 19111.
[30] D. Li, Q.F. Kuang, X.L. Men, B. Zhang, J.Q. Huang, X.L. Shang, B. Yang, T. Yang, Z.W. Li, Z.D. Zhang, J. Mater. Sci. Technol. 198 (2024) 98.
[31] Q.F. Kuang, B. Zhang, B.J. Dong, X.L. Men, B. Yang, Y.T. Zhou, Z.W. Li, X.L. Shang, T. Yang, J.Q. Huang, D. Li, Z.D. Zhang, J. Appl. Phys. 137 (2025) 013908.
[32] Y.L. Yang, J.Y. Ji, J.S. Feng, S.Y. Chen, L. Bellaiche, H.J. Xiang, J. Am. Chem. Soc. 144 (2022) 14907.
[33] B. Zhang, Y. Zhang, Z. Wang, D. Yang, Z. Gao, D. Wang, Y. Guo, D. Zhu, T. Mori, Dalton Trans. 45 (2016) 16561.
[34] L. Septiany, D. Tulip, M. Chislov, J. Baas, G.R. Blake, Inorg. Chem. 60 (2021) 15151.
[35] Q.L. Jiang, J. Zhang, Z.Q. Mao, Y. Yao, D.K. Zhao, Y.H. Jia, D.H. Hu, Y.G. Ma, Adv. Mater. 34 (2022) e2108103.
[36] Z. Yu, H. Peng, Q. Wei, T. Huang, S. Yao, Y. Tian, C. Peng, B. Zou, Mater. Today Chem. 24 (2022) 100781.
[37] G.H. Xu, C. Wang, P. Guo, Acta Cryst. 65 (2009) m171.
[38] C. Dong, J. Appl. Cryst. 32 (1999) 838.
[39] S. Jin, X. Fan, X. Wu, R. Sun, H. Wu, Q. Huang, C. Shi, X. Xi, Z. Li, X. Chen, Chem. Commun. 53 (2017) 9729.
[40] T. Roisnel, J. Rodriguez-Carvajal, Mater. Sci. Forum 378 (2001) 118.
[41] J. Rodriguez-Carvajal, in: Proceedings to the Satellite Meeting on Powder Diffraction of the XV Congress of the IUCr, Toulouse, France, 1990, p. 127.
[42] D. Li, D.S. Pan, W.L. Liu, X.X. Li, M.L. Chen, S.J. Li, Y. Li, J. Tan, D.M. Sun, Z.H. Wang, Z. Han, Z.D. Zhang, Chem. Mater. 29 (2017) 842.
[43] B.W. Park, B. Philippe, X. Zhang, H. Rensmo, G. Boschloo, E.M.J. Johansson, Adv. Mater. 27 (2015) 6806.
[44] E.D. Feng, T.T. Zheng, X.X. He, J.Q. Chen, Q.Y. Gu, X. He, F.H. Hu, J.H. Li, Y. Tian, Angew. Chem. Int. Ed. 62 (2023) e202309249.
[45] S.I. Shylin, V. Ksenofontov, S.J. Sedlmaier, S.J. Clarke, S.J. Cassidy, G. Wortmann, S.A. Medvedev, C. Felser, Europhys. Lett. 109 (2015) 67004.
[46] N.F. Mott, Philos. Mag. 22 (1970) 7.
[47] H.Y. Xie, X.L. Su, T.P. Bailey, C. Zhang, W. Liu, C. Uher, X. Tang, M.G. Kanatzidis, Chem. Mater. 32 (2020) 2639.
[48] X.W. Yan, M. Gao, Z.Y. Lu, T. Xiang, Phys. Rev. Lett. 106 (2011) 087005.
[49] X. Guan, W. Feng, X. Wang, R. Venkatesh, J. Ouyang, ACS Appl. Mater. Interfaces 12 (2020) 13013.
[50] B.L. Zink, J. Magn. Magn. Mater. 564 (2022) 170120.
[51] M. Wu, J. Rhee, T.J. Emge, H. Yao, J.H. Cheng, S. Thiagarajan, M. Croft, R. Yang, J. Li, Chem. Commun. 46 (2010) 1649.
[52] N.W. Ashcroft, N.D. Mermin, in: Solid State Physics, Holt, Rinehart and Winston, New York, 1976, p. 462.
[53] S.S. Yan, in: Y.M. Zhou (Ed.), Solid State Physics Fundamentals, Beijing University Press, Beijing, 2011, p. 140.
[54] Z.D. Zhang, J. Mater. Sci. Technol. 44 (2020) 116.
[55] X.X. Zhang, J. Tejada, J.M. Hernandez, R.F. Ziolo, Nanostruct. Mater. 9 (1997) 301.
[56] J. Cheng, Q. Feng, X. Li, J. Yang, J. Phys. Chem. Lett. 14 (2023) 5048.
[57] X. Li, J. Yang, J. Phys. Chem. Lett. 10 (2019) 2439.
[58] K. Kubota, M. Koshimizu, H. Saito, K. Asai, Bull. Chem. Soc. Jpn. 88 (2015) 1567.
[59] R. Dong, Z. Zhang, D.C. Tranca, S. Zhou, M. Wang, P. Adler, Z. Liao, F. Liu, Y. Sun, W. Shi, Z. Zhang, E. Zschech, S.C.B. Mannsfeld, C. Felser, X. Feng, Nat. Commun. 9 (2018) 2637.
[60] X. Wang, H. Wang, D. Pan, T. Keiper, L. Li, X. Yu, J. Lu, E. Lochner, S. Von Molnar, P. Xiong, J. Zhao, Adv. Mater. 27 (2015) 8043.
[61] S. Hatamie, M.V. Kulkarni, S.D. Kulkarni, R.S. Ningthoujam, R.K. Vatsa, S.N. Kale, J. Magn. Magn. Mater. 322 (2010) 3926.
[62] L. Kang, C. Ye, X. Zhao, X. Zhou, J. Hu, Q. Li, D. Liu, C.M. Das, J. Yang, D. Hu, J. Chen, X. Cao, Y. Zhang, M. Xu, J. Di, D. Tian, P. Song, G. Kutty, Q. Zeng, Q. Fu, Y. Deng, J. Zhou, A. Ariando, F. Miao, G. Hong, Y. Huang, S.J. Pennycook, K.-T. Yong, W. Ji, X.R. Wang, Z. Liu, Nat. Commun. 11 (2020) 3729.
[63] P. Gütlich, J. Ensling, in: Handbook of Analytical Techniques, John Wiley & Sons, Hoboken, 2001, p. 561.
[64] X.F. Lai, Z.P. Lin, K.J. Bu, X. Wang, H. Zhang, D.D. Li, Y.Q. Wang, Y.H. Gu, J.H. Lin, F.Q. Huang, RSC Adv. 6 (2016) 81886.
[65] X.Y. Wang, W.T. Wang, C. Yang, D. Han, H.Z. Fan, J.C. Zhang, J. Appl. Phys. 130 (2021) 170902.
[66] J.W. Yoo, R.S. Edelstein, N.P. Raju, D.M. Lincoln, A.J. Epstein, J. Appl. Phys. 103 (2008) 07B912.